Material Informatics Driven Design and Experimental Validation of Lead Titanate as an Aqueous Solar Photocathode

Taylor Moot[1,†], Olexandr Isayev[2,†], Robert W. Call[3], Shannon M. McCullough[1], Morgan Zemaitis[1], Rene Lopez[3], James F. Cahoon*[,1,] Alexander Tropsha*[,2]

[†] Equal contribution

* Corresponding authors; email: A.T. (alex_tropsha@unc.edu) or J.F.C. (jfcahoon@unc.edu)

[1]Department of Chemistry, University of North Carolina at Chapel Hill, Chapel Hill, NC 27599-3290, USA. [2]Laboratory for Molecular Modeling, UNC Eshelman School of Pharmacy, University of North Carolina at Chapel Hill, Chapel Hill, North Carolina 27599-7360, USA. [3]Department of Physics and Astronomy, University of North Carolina at Chapel Hill, Chapel Hill, NC 27599, USA.

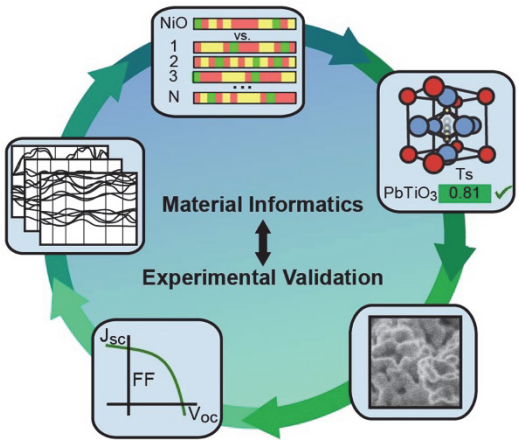

Abstract

Materials informatics is a rapidly emerging data- and knowledge-driven approach for the identification of novel materials for a range of applications, including solar energy conversion. Despite significant experimental effort, the development of highly efficient, stable, and cost-effective photovoltaic materials remains a challenging scientific problem. The quest for precisely-defined semiconductor properties revolves around an immensely broad landscape of structural parameters. Here, we have resolved this challenge by applying material informatics to design a novel photocathode material for dye-sensitized solar cells (DSSCs). By conducting a virtual screening of 50,000 known inorganic compounds, we have identified lead titanate ($PbTiO_3$), a perovskite, as the most promising photocathode material. Notably, lead titanate is significanty different from the traditional base elements or crystal structures used for photocathodes. The fabricated $PbTiO_3$ DSSC devices exhibited the best performance in aqueous solution, showing remarkably high fill factors compared to typical photocathode systems. The results highlight the pivotal role materials informatics can play in streamlining the experimental development of materials with the desired properties.

Introduction

The discovery of new materials with previously unknown or unexpected properties often leads to paradigm shifts in well-established research fields. Examples include the discovery of high-temperature superconductivity, organo-lead halide perovskite solar cells, and antibiotics[1–3]. Historically, such discoveries have often been serendipitous, involving a combination of intuition and the Edisonian approach, because of difficulties with predicting a material's properties or

reverse engineering materials with desired properties. The Edisonian approach is inefficient for exploring a broad landscape of cross-correlated parameters, and therefore, it fails to spot many unexplored materials with potentially unique properties[4]. Resent studies estimate number of chemically feasible quarternary inorganic compounds between 10^{10} and 10^{13} [5,6]. Given the large number of candidate materials, it is impossible to synthesize and evaluate all possible experimental conditions or device configurations. An analogous problem is faced by the drug industry, where computational medicinal chemistry and cheminformatics approaches rely on virtual screening of chemical libraries for rational discovery of novel bioactive compounds[7–11]. Thus, emerging materials-informatics approaches offer an opportunity to leverage available databases and transform the serendipitous discovery process into a data- and knowledge-driven rational design and synthesis strategy, which can accelerate the identification of materials with desired properties[12–22].

The development of solar-energy materials is an example of a challenge where a particularly stringent set of materials properties must be satisfied to achieve high solar-to-electric power-conversion efficiencies (PCEs). For the dye sensitized solar cell (DSSC) research community, a long-standing problem has been the low performance of the p-type solar cells and photocathode materials, which are needed for tandem devices[23,24]. Typically p-type DSSCs use NiO as the photocathode, but there has not been a sustained rise in PCE above 4% since the initial report in 1999 in part due to the consistently low fill factor[25–30]. Newer photocathodes have focused on a relatively small subset of potential semiconductors chosen primarily by their similarity in crystal structure (*e.g.* delafossites) or elemental composition (*e.g.* Cu(I))[31–36]. Despite significant effort to replace NiO, thus far no candidate material has surpassed NiO in overall performance metrics.

Here, we have applied materials informatics to this problem and employed a virtual screening of ~50,000 materials representing a majority of known stoichiometric inorganic compounds. This unique computational exercise was enabled by the use of novel materials descriptors reported in our recent publication[37]. We have identified $PbTiO_3$, which does not contain any typical features characteristic of a p-type DSSC, as the top computational "hit" material[37]. Experimentally fabricated p-type DSSC devices demonstrated record fill factors when $PbTiO_3$ was used with an aqueous electrolyte. The success of this proof of concept study opens the door for the expansive use of materials informatics, relying on materials descriptors, for designing novel compounds with improved physical chemical properties for a wide range of applications[37].

Experimental Methods

Material Fingerprints. Using our recent approach, we encoded the electronic structure diagram for each material as band structure fingerprints[37]. Along every special *k*-point along the wave-vector, the energy diagram was discretized into 32 bins serving as our fingerprint array. It is worth emphasizing that each of the 14 different Bravais lattices has a unique set of *k*-points. The comparison of a set of *k*-points belonging to a single Bravais lattice type will be considered a symmetry-dependent band structure fingerprint. To name a few examples, the Brillouin zone path of a Cubic Lattice (*Γ–X–M–Γ–R–X|M–R)* will be encoded with just four points (*Γ, M, R, X)* giving rise to a fingerprint array of length 128. Body-centered orthorhombic lattice is much more complex (Γ–*X–L–T–W–R–*X_1*–Z–Γ–Y–S–W|*L_1*–Y|*Y_1*–Z*) and represented by 13 points (Γ, L, L_1, L_2, R, S, T, W, X, X_1, Y, Y_1, Z) or fingerprint array of length 416. Conversely, the comparison of identical *k*-points not specifically belonging to any Bravais lattice is always possible when considering the Γ point as it is common to all lattice types. In present work, we limited our

models only to the Γ point of the band structure fingerprint.

Similarity Search. Among many chemical similarity metrics used in cheminformatics, Tanimoto similarity coefficient, T_c, between chemicals A and B is the most widely used[38]. It is calculated as shown in eq. 1,

$$Tc=j=1nxjAxjBj=1n(xjA)2+j=1n(xjB)2-j=1nxjAxjB \quad (1)$$

where x_j is the value of the j^{th} descriptor and n is the total number of descriptors. Tanimoto similarities range from 0.0 (no similarity between chemicals A and B) to 1.0 (A and B are identical). The known p-type photocathodes NiO, Co_3O_4, Cu_2O, CuI, $CuAlO_2$, $CuGaO_2$, $NiCo_2O_4$, and $ZnCo_2O_4$ were used as reference query materials.

Data Sources. We extracted band structure data for 46,936 materials from the AFLOWLIB repository, which represents approximately 60% of known stoichiometric inorganic materials listed in the Inorganic Crystal Structure Database (ICSD)[15,39]. All referenced DFT calculations were performed with the generalized gradient approximation (GGA) PBE exchange-correlation (XC) functional and projector-augmented wavefunction (PAW) potential according to the AFLOW standard for high-throughput computing[40]. This standard ensures reproducibility of the data, as well as provides visibility and reasoning for any parameter set used in calculations, such as accuracy thresholds, calculation pathways, and mesh dimensions.

$PbTiO_3$ Film Fabrication. All reagents were purchased from Fisher Scientific and used without further purification unless noted otherwise. In an inert, dry atmosphere lead acetate anhydrous (0.075 g) was combined with glacial acetic acid (2 mL). Then, titanium isopropoxide (0.05 mL) was combined with anhydrous ethanol (8 mL). The two solutions were combined and the resulting sol was capped and removed from the glove box. To create structured films, 10 wt.% ethyl cellulose (22 cp) was added to the precursor sol solution. A drop of the sol gel

solution was wiped across fluorine doped tin oxide (FTO) glass substrates (12-14 Ω/cm^2) purchased from Hartford glass (TEC15) and cleaned with typical organic solvents and sonication. To make thin films, 5 layers of the sol solution were spun onto FTO glass substrate, with a 1 minute 150 °C heat treatment between each layer. All films were then annealed in air for 70 minutes at 600 °C then cooled to room temperature.

DSSC Assembly. Processed films were submerged in a 0.5 mM P1 (Dynamo) in acetonitrile solution for 20 minutes. Pt counter electrodes were fabricated by drop-casting H_2PtCl_6 in isopropanol solution onto an FTO glass slide, which included a powder-blasted pinhole, and annealing for 30 minutes at 380 °C. The DSSC was fabricated by sandwiching a 20 μm Surlyn polymer gasket (Solaronix) between the working P1 dyed $PbTiO_3$ electrode and the Pt counter electrode using a custom-built heating apparatus. The devices were backfilled with electrolyte using a custom-built vacuum chamber. The electrolyte consists of 1.0 M LiI and both the solvent and the amount of I_2 was varied as noted in text. The pinhole was sealed with a microscope coverslip and additional Surlyn polymer.

Analytical Methods. Film morphology, thickness, and crystal structure were measured with a Hitachi S-4700 cold-cathode field-emission scanning electron microscope (SEM), a Bruker DektakXT profilometer, and a Rigaku Multiflex x-ray diffractometer with Cu source, respectively. X-ray diffraction spectra were collected from 20°-60° 2θ at a scan rate of 2° 2θ/min. Transmission electron microscopy (TEM) and scanning TEM (STEM) images were obtained with an FEI Tecnai Osiris operating at 200 kV with a sub-nanometer probe and equipped with a Super-X EDS system. This system was used to acquire drift-corrected energy dispersive x-ray spectroscopy (EDS) elemental maps of $PbTiO_3$ particles using the Bruker Esprit software, and standardless Cliff-Lorimer analysis was performed on the deconvoluted EDS

spectra for elemental quantification. Optical properties of each film were measured in a Cary 5000 UV−Vis−NIR from Agilent with integrating sphere attachment. Dye desorption measurements and the absorption profile of dye-loaded films in solution were taken using a Hewlett-Packard UV-Vis-NIR absorption spectrometer HP 8453. Macroscale pictures were taken using an iPhone 5c. Fluorescence measurements were performed on dye-loaded films using a 532 nm laser coupled to a Nikon D-Eclipse C1 SI microscope with a CCD detector. EIS and Mott-Schottky analysis were done using a Gamry Reference 600 electrochemical impedance spectrometer. EIS was performed on DSSCs under 1-sun illumination at an applied bias, and the resulting curves were fit to a simplified Randles circuit using the Gamry Software. Mott-Schottky analysis was done at 10 Hz and 5 Hz in a three-electrode configuration with a Pt mesh counter electrode and an Ag/AgCl reference electrode in a 0.1 M $LiClO_4$ solution with varying water percentages. The large linear portion of $1/C^2$ was fit with a linear function, where the *x*-intercept was determined to be the V_{fb}, and the slope was converted to doping level as follows from the equation: $1C2=2\varepsilon 0\varepsilon RA2qND(V-Vfb-KBTq)$. Cyclic voltammograms were collected with a Pine WaveNow Potentiostat at a scan rate of 100 mV/s with a glassy carbon working electrode, Pt wire counter electrode, and an Ag/AgCl reference electrode. DSSC performance was investigated using a Newport Oriel 150W class ABB solar simulator with an AM1.5G filter. The light intensity was calibrated to 1-sun using a certified reference solar cell (Newport 91150 Vs), which was calibrated in June, 2011. A Keithley 2636A SourceMeter was used for all electrical measurements. All photovoltaic performance measurements were done in air at room temperature with a step size of +1 mV in the increasing forward bias direction (except where explicitly stated otherwise in Figure S7) and a 0.1 second delay. Average values and standard deviations for DSSC photovoltaic device metrics represent measurements on 7-10

separate devices, as noted in Table S2. The average active area of the devices is 0.42 ± 0.06 cm^2. The active area of each device was equivalent to the size of the gaskets used to hold the liquid electrolyte; thus, no aperture or mask was used during illumination. Incident photon-to-current efficiency (IPCE) measurements were obtained by illuminating devices with a Newport Instruments tungsten lamp coupled to a Princeton Instruments SP-2300 spectrometer with 1200 g/mm grating. A comparison of the J_{SC} values calculated from IPCE spectra and collected during 1-sun illumination is provided in Table S6. Note that the key metrics discussed, V_{OC} and fill factor, are not substantially affected by minor changes in light absorption and J_{SC}. The photovoltaic performance has not been confirmed by an independent certification laboratory. All errors and error bars represent one standard deviation.

Results and Discussion

Virtual Screening and Materials Similarity in Electronic Structure Space. Tracing back to the ancient "like dissolves like" principle, the concept of similarity is one of the most common rational principles of deducing new knowledge based on existing knowledge. For pharmaceuticals, this concept is predicated on the basic idea of the Similar Property Principle, which states that molecules that are structurally similar are likely to have similar properties[41–44]. When identifying new materials with the desired property, the knowledge-driven approach would entail searching for materials with crystal structures similar to that for a known material with the same property. For materials, however, this principle is not sufficient and additional characteristics, in particular the similarity of electronic band structures, are likely to be as or more important than crystal structure similarity. In addition, quantifying similarity is another

non-trivial task requiring the definition of unique characteristics (descriptors) of individual materials and the design of specific similarity metrics.

As illustrated in Figure 1, we have developed a robust knowledge-driven approach for the discovery of novel p-DSSC materials using our recently-introduced materials descriptors that encode band structures (B-fingerprints)[37]. In the B-fingerprint, a material's energy band diagram is discretized into 32-bit vector representations, where each Brillouin zone has a unique set of high-symmetry points that together give rise to a symmetry-dependent fingerprint (see Figure S1 and Methods for a detailed explanation). Known photocathodes, such as NiO or Cu_2O, were used as reference query materials; their band structures were calculated with the density functional theory (DFT) PBE functional and converted into B-fingerprints. We assume that multiple semiconductor properties that give rise to good p-type DSSC performance will be implicitly encoded within the B-fingerprint material descriptors[45,46]. To identify new materials, we performed a virtual screening with the AFLOWLIB database of ~50,000 inorganic compounds to identify the top three "hit" materials for each reference query (see Supplementary Table S1)[15,47]. The similarity was assessed with the Tanimoto coefficient, T_c as described in Methods.

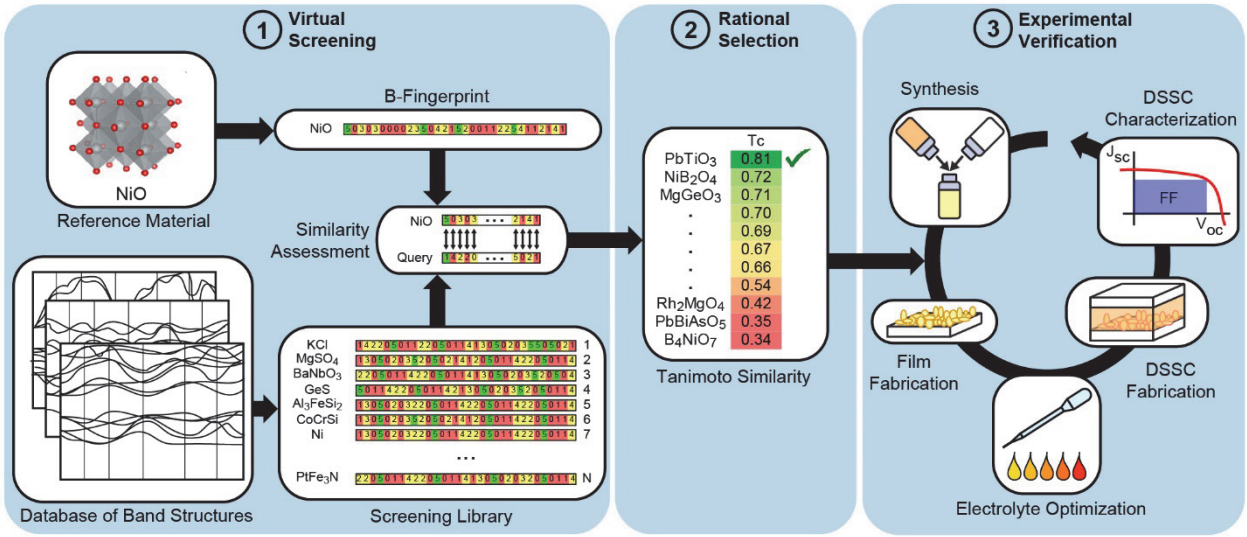

Figure 1 | General knowledge-driven workflow. The process involves (1) virtual screening of materials using B-fingerprints for similarity assessment, (2) rational selection of top candidate materials, and (3) experimental verification through an iterative process of material synthesis, film fabrication, and electrolyte optimization to obtain the best DSSC performance characteristics.

Out of the ca. 50,000 materials in the database, about 3,400 are in the acceptable range of band gap and over 1,900 have a compatible valence band edge position. Therefore, simple filtering criteria are not sufficiently selective to prioritize a single material for experimental validation. Among the twenty materials with the highest T_c values, two perovskite ($BaMnO_3$ and $PbTiO_3$) and two spinel ($MnFe_2O_4$ and $NiCr_2O_4$) materials exhibited a high degree of B-fingerprint similarity to several of the query materials. The four selected material candidates were further ranked according to the properties typically used to vet potential photocathodes: stability, synthetic feasibility, and transparent color (band gap >3 eV).

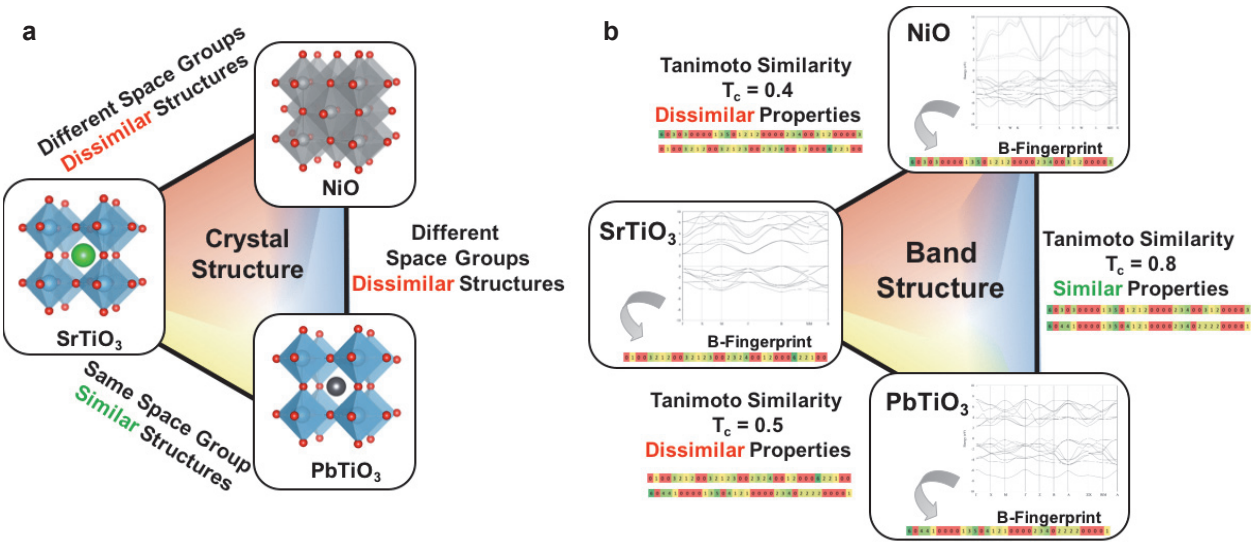

Figure 2 | Assessment of similarity between NiO, $PbTiO_3$ and $SrTiO_3$. The comparison is based on **a**, structural geometry and **b**, electronic band structure using B-fingerprints.

As expected, the materials identified through virtual screening are similar in terms of their electronic band structure but not similar in terms of either geometric structure or elemental composition, *i.e.*, most commonly considered materials properties, as illustrated by the examples in Figure 2. For instance, $PbTiO_3$ and $SrTiO_3$ are structural analogues (Figure 2a) with a perovskite structure; however, their electronic structure properties are dissimilar, yielding a relatively low T_c of 0.5 (Figure 2b). In contrast, NiO and $PbTiO_3$ do not appear similar based on their elemental composition or crystal structure (Figure 2a). However, they are similar by their band structure (Figure 2b), as reflected by their relatively high T_c of 0.8.

$PbTiO_3$ was selected as a top choice because it was identified as the most similar to NiO among all screened materials based on B-fingerprint representation with a T_c of 0.8. Based on the DFT calculations, the valence band position of $PbTiO_3$ is similar to NiO (−5.02 eV vs vacuum), with a large band gap (3.96 eV). This allows for efficient hole injection from standard p-DSSC chromophores and minimal deterious semiconductor absorption, respectively. Lead titanate is known to be a ferroelectric and have a high dielectric constant (ε~200); both of these properties have been noted as potentially beneficial for photovoltaics[48]. In addition, the perovskite crystal structure is analogous to $SrTiO_3$, a well-known photoanode material, as well as the organolead materials reaching record PCEs of over 20%[49]. Other computational studies show a high calculated hole mobility for $PbTiO_3$[21].

However, the choice of $PbTiO_3$ is not particularly obvious when considering all 1,900 potential candidates. Traditionally, scientists looked into materials analogous to NiO, such as 3*d*

transition metal oxides, but with a property that is clearly advantageous. For instance, a deeper valence band position could produce a larger open-circuit voltage (V_{OC}) in DSSCs[28,34]. Cu delafossites have recently been highlighted because they have a hybrid metal-oxygen valence band character which is favorable to hole transport[36]. Finally, any new material to be used as a photocathode also requires a nanoparticle synthesis method with a low sintering temperature that will maintain a high surface area electrode for high chromophore loading and therefore a high short-circuit current density (J_{SC}).

There are no obvious markers that indicate $PbTiO_3$ would outperform NiO. The oxidation states of Pb and Ti make it ambiguous which metal vacancy will act as a dopant, and literature suggests a nearly intrinsic doping level, lending uncertainty as to p- or n-type behavior[50]. A comparison of crystal structures points to the well-known photoanode $SrTiO_3$, which requires aggressive synthetic conditions to introduce dopants[51]. $PbTiO_3$ has a similar DFT-calculated valence band edge to NiO, so there would be no improvement in V_{OC}. Finally, a high sintering temperature would limit surface area and therefore J_{SC}[52]. The lack of clear advantageous properties, coupled with the apparent synthetic difficulty of a highly-doped, high surface area material, $PbTiO_3$ would not be seen as a good candidate. Thus, $PbTiO_3$ represents a good test case to see how materials informatics can successfully identify a non-obvious but promising new material that is worthy of continuing study. As a critical component of this approach, the similarity search in the electronic structure space allows for unique hypothesis generation and prioritization of material candidates without the typical bias arising from known structural prototypes or specific emphasized parameters.

$PbTiO_3$ Experimental Results

$PbTiO_3$ has been widely explored for its ferroelectric properties but has not been widely investigated for solar-energy applications[53]. A modified sol-gel synthesis (see Methods) was used to prepare white, porous, and compositionally-uniform films of $PbTiO_3$ on conductive glass substrates, as shown by the optical and electron microscopy images in Figure 3[52,54–56]. The porous films are ~700 nm thick (see profilometry measurements in Figure S2) and composed of grains ~30-300 nm in size, as shown by the scanning electron microscopy (SEM) image in Figure 3a. The as-deposited films visually appear white and opaque (upper image in Figure 3b), which is consistent with scattering caused by the large size distribution of particles within the film. Transmission electron microscopy (TEM) imaging and energy dispersive x-ray spectroscopy (EDS) mapping of an agglomerate of particles (Figure 3c) show that the material is compositionally uniform with a Pb:Ti ratio of 1.1:1.0. In addition, the x-ray diffraction (XRD) spectrum in Figure 3d shows strong diffraction peaks consistent with perovskite crystal structure of phase-pure, crystalline $PbTiO_3$[55]. Absorption data and a Tauc plot (Figure 3e) confirm that the direct bandgap of the material is ~3.3 eV, similar to other literature reports[55]. In order to examine the DSSC performance of $PbTiO_3$, films were dye loaded with the organic chromophore denoted P1[61], yielding bright red films (lower image in Figure 3b). A dye loading of ~5 nmol/cm^2 (Figure S3) was measured, which is approximately one-third of that typically reported for P1 on NiO at similar film thicknesses[57,58].

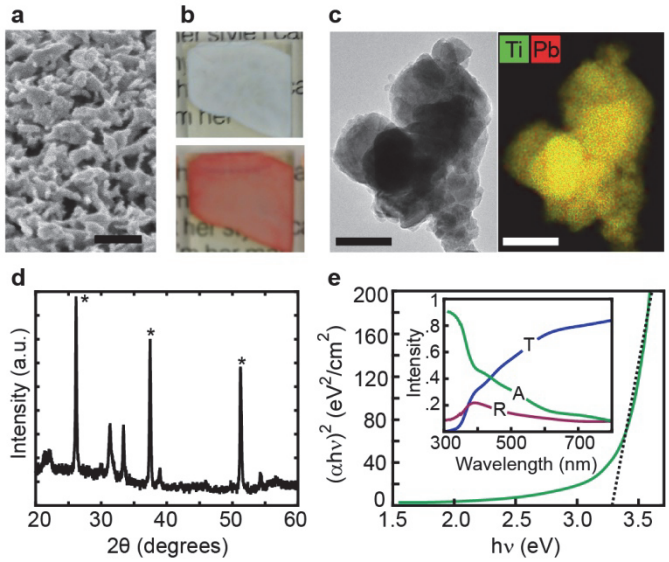

Figure 3 | Characterization of porous $PbTiO_3$ films. **a**, SEM image of a $PbTiO_3$ film with grains 30-300 nm; scale bar: 200 nm. **b**, Photograph of a $PbTiO_3$ film ~700 nm thick on a glass slide before dye loading (upper) and after dye loading (lower) with the organic chromophore P1. **c**, TEM image (left) and EDS STEM map (right) of a nanoparticle aggregate from a $PbTiO_3$ film, showing Ti in green and and Pb in red with a Pb:Ti ratio of 1.1:1.0; scale bar: 50 nm. **d**, XRD spectrum of $PbTiO_3$ on FTO glass. Peaks from FTO are denoted with *. **e**, Tauc plot for $PbTiO_3$ with a direct bandgap of ~3.3 eV. Dashed line represents a linear fit of the data. Inset: absorptance (green), reflectance (purple), and transmittance (blue) data of a $PbTiO_3$ film ~700 nm thick.

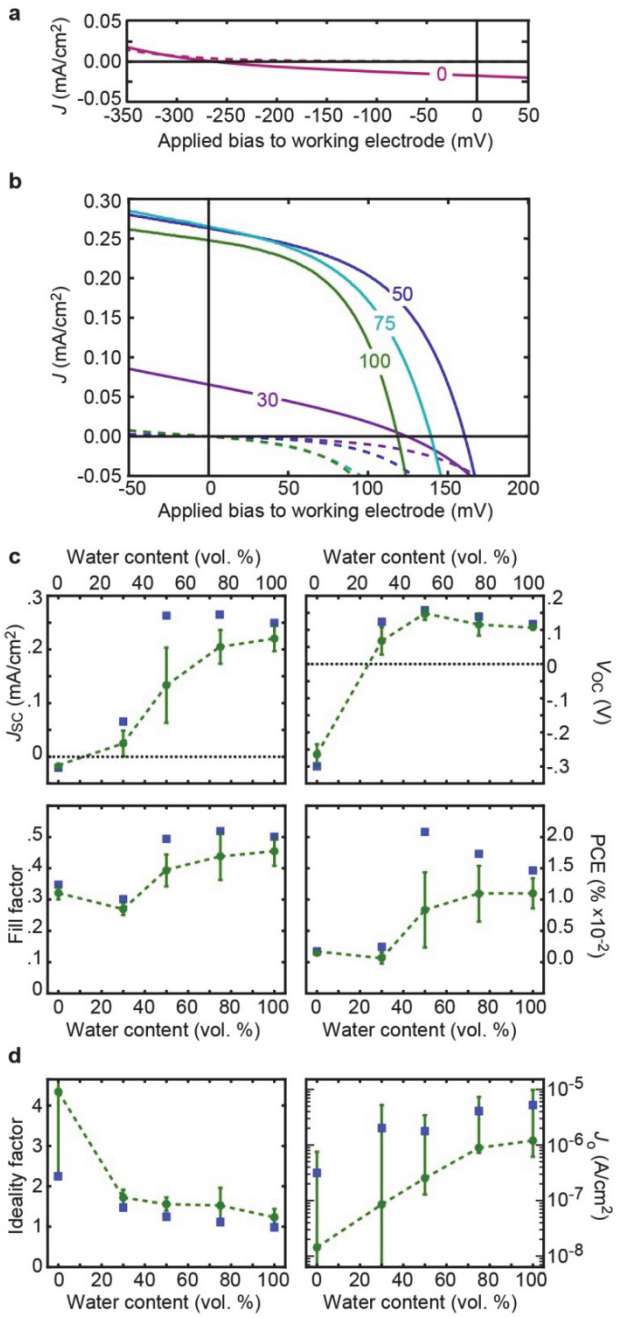

Figure 4 | Photovoltaic characteristics of $PbTiO_3$ in water/acetonitrile solutions. a, Photoanodic *J-V* curves for the champion $PbTiO_3$ DSSC devices in an acetonitrile electrolyte solution under 1-sun illumination (solid line) and in the dark (dashed line). **b,** Photocathodic *J-V* curves for champion $PbTiO_3$ DSSC devices under 1-sun illumination (solid lines) and in the dark (dashed lines) where labels denote the volume percent water. Pink, purple, dark blue, light blue,

and green curves represent 30, 50, 75, and 100 volume percent water, respectively. In panels a and b, negative J_{SC} values represent photoanodic current whereas positive J_{SC} values represent photocathodic current. **c**, Photovoltaic metrics of DSSC devices as a function of the water content, showing the J_{SC} (upper left), V_{OC}, (upper right), fill factor (lower left), and PCE (lower right). Blue squares denote champion devices and green circles denote average values. **d**, Dark photovoltaic metrics of DSSC devices as a function of the water content, showing the ideality factor (left) and J_o, dark saturation current, (right).

Initial DSSC devices were fabricated with the I^-/I_3^- electrolyte in acetonitrile using 0.1 M I_2 and 1.0 M LiI. However, the pure acetonitrile-based devices produced photoanodic current under 1-sun illumination, as shown by the current density-voltage (*J-V*) curve in Figure 4a. This result is the opposite of our expectations based on valence band edge derived from DFT calculations. However, it is known that the semiconductor/electrolyte interface can substantially alter the effective band edge position, so we explored alternate electrolyte solutions. Acetonitrile is an aprotic solvent, but the introduction of protons can significantly shift the band edge position through protonation/deprotonation equilibrium at the interface[59–61]. Thus, we introduced water into the electrolyte solution to probe the effect on device performance. Note that films in acetonitrile exhibited some desorption of dye but did not in aqueous solution, which is consistent with the limited solubility of P1 in water (Figure S4).

J-V characteristics of champion $PbTiO_3$ DSSC devices in the dark and under 1-sun illumination are shown in Figure 4b, and trends in photovoltaic metrics for various ratios of acetonitrile and water are shown in Figure 4c. All metrics are tabulated in Tables S2 and S3. Figure S5 displays *J-V* curves characteristic of average performance, and minimal hysteresis was

observed in the *J-V* curves (Figure S6). Notably, the J_{SC} changes sign between 0 and 30% water and then plateaus at 0.2-0.3 mA/cm^2 for 75% water and above. The V_{OC} of photocathodic devices reaches a maximum of 146 mV in 50% water and then decreases to a maximum of 109 mV in 100% water. The fill factor increases with water content, and a champion fill factor above 50% is measured for both 75% and 100% water. Finally, the increase in fill factor, coupled with the increase in J_{SC}, improves the PCE tenfold when changing from a pure acetonitrile to pure water solution.

The change in the sign of J_{SC} upon the addition of 30% water to acetonitrile indicates shift from photoanodic to photocathodic behavior, where the cathodic behavior was maintained with increasing water percentages. Contrary to observations with TiO_2 aqueous DSSCs, $PbTiO_3$ devices have a higher PCE in an aqueous environment compared to acetonitrile, which is advantageous for future development of humidity-stable DSSCs and water-splitting solar fuel devices[62,63].

The V_{OC} values obtained from $PbTiO_3$ with 50% water or higher are comparable to those obtained from NiO[29,57]. The slight decrease in V_{OC} above 50% water is correlated with an increase in the dark saturation current density J_o (Figure 4d, right) which is likely due to a change in the I_2/I_3^- equilibrium constant, which shifts the electrolyte Nernst potential more positive on the electrochemical scale by ~0.2 V from 0% to 100% water (Figure S7). In addition, the average ideality factor of the devices (Figure 4d, left) decreases from 1.56 to 1.23 when moving from 50% to 100% water, which may also contribute to a decrease in V_{OC}[63]. The high fill factors of the devices, with a champion value of 52% in 75% water, is ~50% larger than the values typically measured from NiO and is a record for p-type DSSC devices using P1 and an iodide-based electrolyte[27,29]. The maximum theoretical fill factor, based on a V_{OC} of ~150 mV, is

estimated to be ~58% (Figure S8), indicating that ~90% of the potential power is generated given the available photocurrent and photovoltage.

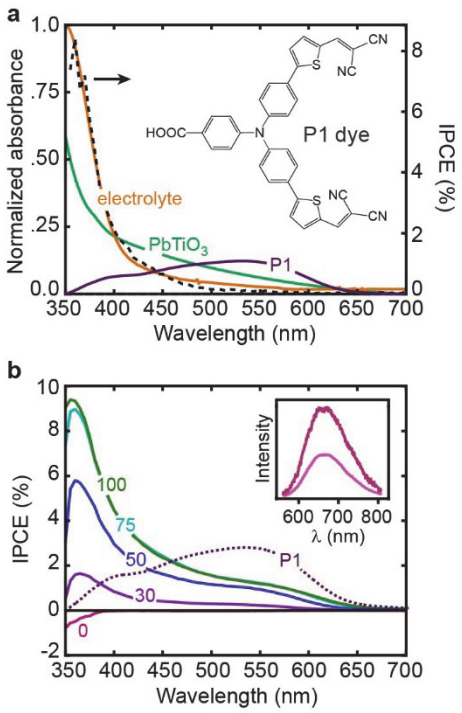

Figure 5 | Photoresponse of dye-loaded $PbTiO_3$ films and devices. a, Left-hand axis: absorbance spectra of the $PbTiO_3$ film (green), the 100% water electrolyte solution (orange), and the P1 chromophore on the $PbTiO_3$ surface in 100% water electrolyte solution (purple). The P1 peak red shifts from 495 to 508 to 532 nm when changing between the dry state, pure water, and electrolyte solution, respectively. Values are normalized to the maximum intensity across all spectra. Right-hand axis: IPCE spectrum (dashed black line) of a solar cell device without dye in 100% water electrolyte solution. Inset: molecular structure of the P1 chromophore. **b**, IPCE spectra of DSSC devices with 0 (pink), 30 (purple), 50 (dark blue), 75 (light blue), and 100 (green) volume percent water. Dashed black line is the absorption spectrum of the P1 chromophore as shown in panel a. Inset: fluorescence signal from the P1 chromophore on glass

(red) and on the $PbTiO_3$ film (black). The intensity is normalized to the peak absorption value of the P1 chromophore in the visible range.

The origin of the J_{SC} values and changes in J_{SC} with water content were investigated by measuring the wavelength-dependent photoresponse of the $PbTiO_3$ films and devices. Absorption spectra of the $PbTiO_3$ film, electrolyte solution, and the P1 chromophore loaded onto $PbTiO_3$ films are shown in Figure 5a. An incident photon to current efficiency (IPCE) spectrum of a device without a dye in 100% water is shown as the dashed black line in Figure 5a. The device without dye produces a J_{SC} of 0.06 mA/cm^2 (Figure S9) and exhibits an abruptly increasing IPCE spectrum below 400 nm that matches the absorption profile of the electrolyte. The generation of photocurrent from the electrolyte was confirmed by varying the I_2 concentration in devices, showing an increase in photocurrent with increasing I_2 concentration (Figure S10), a result that is consistent with other p-type devices[28,29,32].

IPCE spectra of dye-loaded films at each water percent (Figure 5b) show substantial additional intensity in the visible range, which is consistent with the absorption profile of the P1 chromophore. We estimate that absorption by the P1 chromophore produces ~50% of the measured J_{SC} in the devices. Absorbed photon to current efficiency (APCE) spectra (Figure S11) were also calculated, with an APCE of ~4% at the P1 absorption peak of 532 nm for 100% water. To understand the origin of the low APCE values, fluorescence measurements (inset of Figure 5b) were used to determine if the photoexcited P1 chromophore either injects holes or relaxes back to the ground state via fluorescence. On $PbTiO_3$ films, the fluorescence signal is quenched by only ~50%, which indicates that a large fraction of the photoexcited P1 dye does not inject into the valence band of $PbTiO_3$.

To understand the low injection yield into $PbTiO_3$, we measured the flatband potential (V_{fb}) in various solvent ratios by Mott-Schottky analysis (Figure S12). The V_{fb} was used to estimate the conduction and valence band edges, as shown in Figure 6a. A significant shift of V_{fb} by more than 0.5 eV, from >2 V in pure acetonitrile to 1.51 ± 0.01 V *vs* Ag/AgCl in 30% water, is observed, after which the further addition of water has little impact on V_{fb}. As expected, the more positive electrochemical potential in pure acetonitrile is favorable for electron injection whereas the more negative V_{fb} upon addition of water is more favorable for hole injection. However, the oxidative potential of the P1 excited state still has relatively minimal overlap with the valence band of $PbTiO_3$ even in pure water. Thus, we would expect the rate of hole transfer to the valence band to be slow, which is consistent with the observed fluorescence of P1 and the low J_{SC} and APCE values[64].

Similarly large shifts in the V_{fb} of TiO_2 in water have been observed and explained by the protonation/deprotonation equilibrium at the semiconductor surface[60,61]. Consequently, the addition of water affects the protonation/deprotonation equilibrium on the surface of $PbTiO_3$ and shifts the V_{fb}. Previous reports on $Pb(Zr,Ti)O_3$ solid-state devices have reported a shift from anodic to cathodic performance, which was postulated to be a result of the ferroelectric surface[50]. It should be noted that the theoretical maximum V_{OC} from these V_{fb} is ~1 V, despite the experimental V_{OC} of ~150 mV. This difference cannot be explained by the dark saturation currents (Figure 4d), which are reasonably low at ~5 x 10^{-6} A/cm^2 (Table S3) in all solvents[29]. We suspect that the low photocurrent as well as the large difference between the work function of the metallic back contact and the V_{fb} of $PbTiO_3$ may play a role in diminishing the V_{OC}, as is commonly seen in organic photovoltaic devices[65].

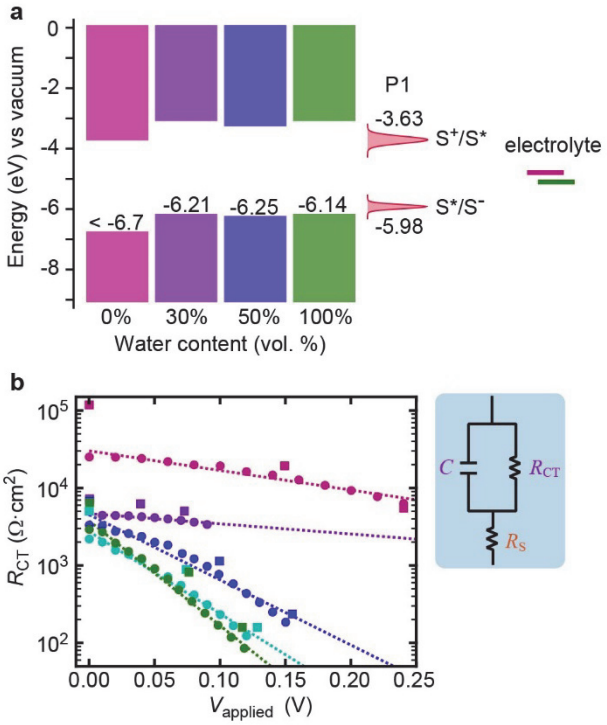

Figure 6 | Analysis of the $PbTiO_3$ DSSC performance. a, Left: schematic of the conduction and valence band edges of $PbTiO_3$ as a function of water content as estimated by averaging 10 Hz and 5 Hz V_{fb} from Mott-Schottky analysis, which is approximated as the valence band edge. Middle: oxidation and reduction potentials, with Gaussian linewidths, of the P1 chromophore as measured in acetonitrile solution[58]. Right: Nernstian potential for the redox couple in acetonitrile (pink) and water (green). All values are reported relative to the vacuum level. **b**, Charge-transfer resistance, R_{CT}, as a function of applied potential as determined by EIS (squares) and by the differential resistance of *J-V* curves (circles) for 0 (pink), 30 (purple), 50 (dark blue), 75 (light blue), and 100 (green) volume percent water. The simplified Randles circuit used to model EIS data is shown on the right, including R_{CT}, interfacial capacitance C, and series resistance R_S.

The change in V_{fb} explains the shift from anodic to cathodic performance but does not fully explain the improved overall performance in water over acetonitrile. We hypothesize that

large changes in the diffuse double layer and dynamics at the semiconductor/electrolyte interface are likely the main causes of increased performance. To further explore this interface, we performed electrochemical impedance spectroscopy (EIS) of DSSC devices (Figure S13). If interpreted using a simplified Randles circuit (Figure 6b), the EIS data indicates there is no substantial change in the series resistance, R_S, but a large change in charge-transfer resistance, R_{CT}, at the semiconductor-solution interface upon the addition of water (see Table S4). The recombination differential resistance, R_{rec}, of the devices, calculated as $(dJ/dV)^{-1}$, is in good agreement with R_{CT}, as shown by the similarity of the data in Figure 6b, indicating $R_{rec} \approx R_{CT}$. R_{rec} shows an exponential dependence on applied voltage and can be fit as[66]:

$$R_{rec} = R_o \exp(-q\beta V/k_B T) ,$$

where β is the recombination coefficient, R_o is a pre-exponential term related to J_o, k_B is the Boltzmann constant, q is elementary charge, and T is temperature. β increases from 0.15 at 0% water to 0.80 in 100% water (Table S5), which corresponds well to the previously measured ideality factors, where $\beta = 1/n$[66]. The increase in β with increasing water concentration suggests a substantial change in the mechanism of recombination at the semiconductor-solution interface and could indicate a decreased role of trap states above the valence band edge[66]. The results highlight the significant role of the interface in determining device performance, and additional investigation will be necessary to elucidate the details of the novel $PbTiO_3$-water system for high-performance DSSC devices[67].

Conclusions

The unique performance features of $PbTiO_3$ p-type DSSCs give rise to many interesting questions about the role of solvent and the semiconductor-electrolyte interface as well as the role

of a high dielectric constant, and related ferroelectricity, as an important material property. The results also point to the need for design and synthesis of chromophores with higher oxidative potentials than P1, which would likely dramatically improve the J_{SC} of $PbTiO_3$ devices and thus the overall PCE. Alternatively, training a machine learning model to predict the work function directly can both improve the screening process and minimize device design issues with currently used chromophores. Beyond these specific questions, this work highlights the utility of material informatics approaches to both identify important semiconductor properties and prioritize previously unexplored materials for experimental studies. This proof-of-concept discovery of a novel DSSC material illustrates the power of materials descriptors that enable the application of the virtual screening approach for rapid and effective identification of diverse materials in large databases with properties similar to those of a query. Because of the complexity and lengthiness of the experimental characterization, only $PbTiO_3$ was investigated here; additional top candidates will be tested in the future. Potentially, the same approach can be used for different DSSC components, such as the chromophore, to ultimately, design each component of the device. In sum, this approach could allow for expedited design of each device component for a highly optimized DSSC. We hope that this investigation will help establishing materials informatics as a common tool to accelerate the design and discovery of novel functional materials with the desired performance characteristics.

Acknowledgements

A.T. acknowledges support from DOD-ONR (N00014-16-1-2311) for the computational studies reported in this paper. Development of the web service (O.I.) was supported by the Russian Scientific Foundation (No. 14-43-00024). T.M., R.W.C, S.M.M, M.E.Z., C.J.F., R.L. and J.F.C.

acknowledge support for all of the experimental studies on PbTiO3 by the UNC Energy Frontier Research Center (EFRC) "Center for Solar Fuels," an EFRC funded by the U.S. Department of Energy, Office of Science, Office of Basic Energy Sciences, under Award DE-SC0001011. This research made use of instrumentation at the Chapel Hill Analytical and Nanofabrication Laboratory (CHANL), a member of the North Carolina Research Triangle Nanotechnology Network (RTNN), which is supported by the National Science Foundation (NSF) (ECCS-1542015) as part of the National Nanotechnology Coordinated Infrastructure (NNCI). We thank J. R. McBride for TEM imaging using instrumentation supported by NSF grant EPS-1004083 (TN-SCORE). We acknowledge the UNC ITS Research Computing Center for access to the KillDevil cluster for computational studies. O.I. also acknowledges computational resources provided by Extreme Science and Engineering Discovery Environment (XSEDE) program, which is supported by NSF grant number ACI-1053575.

References:

1. Park, N. G. Perovskite solar cells: An emerging photovoltaic technology. *Materials Today* **18,** 65–72 (2015).
2. Orenstein, J. Advances in the Physics of High-Temperature Superconductivity. *Science.* **288,** 468–474 (2000).
3. Donadio, S., Maffioli, S., Monciardini, P., Sosio, M. & Jabes, D. Antibiotic discovery in the twenty-first century: current trends and future perspectives. *J. Antibiot. (Tokyo).* **63,** 423–430 (2010).
4. Walsh, A. Inorganic materials: The quest for new functionality. *Nat. Chem.* **7,** 274–275 (2015).

5. Isayev, O., Oses, C., Curtarolo, S. & Tropsha, A. Universal Fragment Descriptors for Predicting Electronic Properties of Inorganic Crystals. 1–12 (2016). at <http://arxiv.org/abs/1608.04782>

6. Davies, D. W. *et al.* Computational Screening of All Stoichiometric Inorganic Materials. *Chem* **1,** 617–627 (2016).

7. Gorse, A.-D. Diversity in medicinal chemistry space. *Curr. Top. Med. Chem.* **6,** 3–18 (2006).

8. Bajorath, J. Integration of virtual and high-throughput screening. *Nat. Rev. Drug Discov.* **1,** 882–94 (2002).

9. Kitchen, D. B., Decornez, H., Furr, J. R. & Bajorath, J. Docking and scoring in virtual screening for drug discovery: methods and applications. *Nat. Rev. Drug Discov.* **3,** 935–949 (2004).

10. Ain, Q. U., Aleksandrova, A., Roessler, F. D. & Ballester, P. J. Machine-learning scoring functions to improve structure-based binding affinity prediction and virtual screening. *Wiley Interdiscip. Rev. Comput. Mol. Sci.* **5,** 405–424 (2015).

11. Heikamp, K. & Bajorath, J. The future of virtual compound screening. *Chem. Biol. Drug Des.* **81,** 33–40 (2013).

12. Curtarolo, S. *et al.* The high-throughput highway to computational materials design. *Nat. Mater.* **12,** 191–201 (2013).

13. Hattrick-Simpers, J., Wen, C. & Lauterbach, J. The Materials Super Highway: Integrating High-Throughput Experimentation into Mapping the Catalysis Materials Genome. *Catal. Letters* **145,** 290–298 (2015).

14. Materials Genome Initiative.

15. Curtarolo, S. *et al.* AFLOWLIB.ORG: A distributed materials properties repository from high-throughput ab initio calculations. *Comput. Mater. Sci.* **58,** 227–235 (2012).

16. Jain, A. *et al.* Commentary: The Materials Project: A materials genome approach to accelerating materials innovation. *APL Mater.* **1,** 011002 (2013).

17. Saal, J. E., Kirklin, S., Aykol, M., Meredig, B. & Wolverton, C. Materials Design and Discovery with High-Throughput Density Functional Theory: The Open Quantum Materials Database (OQMD). *Jom* **65,** 1501–1509 (2013).

18. Hachmann, J. *et al.* The Harvard Clean Energy Project: Large-Scale Computational Screening and Design of Organic Photovoltaics on the World Community Grid. *J. Phys. Chem. Lett.* **2,** 2241–2251 (2011).

19. Kalidindi, S. R. Data science and cyberinfrastructure: critical enablers for accelerated development of hierarchical materials. *Int. Mater. Rev.* **60,** 150–168 (2015).

20. Rajan, K. Materials Informatics: The Materials 'Gene' and Big Data. *Annu. Rev. Mater. Res.* **45,** 153–169 (2015).

21. Hautier, G., Miglio, A., Ceder, G., Rignanese, G.-M. & Gonze, X. Identification and design principles of low hole effective mass p-type transparent conducting oxides. *Nat. Commun.* **4,** 2292 (2013).

22. Raccuglia, P. *et al.* Machine-learning-assisted materials discovery using failed experiments. *Nature* **533,** 73–76 (2016).

23. Hanna, M. C. & Nozik, A. J. Solar conversion efficiency of photovoltaic and photoelectrolysis cells with carrier multiplication absorbers. *J. Appl. Phys.* **100,** (2006).

24. Snaith, H. J. Perovskites : The Emergence of a New Era for Low-Cost , High-Efficiency Solar Cells. *J. Phys. Chem. Lett* **4,** 3623−3630 (2013).

25. He, J., Lindström, H., Hagfeldt, A. & Lindquist, S.-E. Dye-Sensitized Nanostructured p-Type Nickel Oxide Film as a Photocathode for a Solar Cell. *J. Phys. Chem. B* **103,** 8940–8943 (1999).

26. Perera, I. R. *et al.* Application of the tris(acetylacetonato)iron(III)/(II) redox couple in p-type dye-sensitized solar cells. *Angew. Chemie - Int. Ed.* **54,** 3758–3762 (2015).

27. Huang, Z. *et al.* Probing the Low Fill Factor of NiO p-Type Dye-Sensitized Solar Cells. *J. Phys. Chem. C* **116,** 26239–26246 (2012).

28. Odobel, F. *et al.* Recent advances and future directions to optimize the performances of p-type dye-sensitized solar cells. *Coord. Chem. Rev.* **256,** 2414–2423 (2012).

29. Flynn, C. J. *et al.* Site-Selective Passivation of Defects in NiO Solar Photocathodes by Targeted Atomic Deposition. *ACS Appl. Mater. Interfaces* **8,** 4754–4761 (2016).

30. Click, K. A. *et al.* A double-acceptor as a superior organic dye design for p-type DSSCs: high photocurrents and the observed light soaking effect. *Phys. Chem. Chem. Phys.* **16,** 26103–11 (2014).

31. Jiang, T. *et al.* Copper borate as a photocathode in p-type dye-sensitized solar cells. *RSC Adv.* **6,** 1549–1553 (2016).

32. McCullough, S. M., Flynn, C. J., Mercado, C. C., Nozik, A. J. & Cahoon, J. F. Compositionally-tunable mechanochemical synthesis of $Zn_xCo_{3-x}O_4$ nanoparticles for mesoporous p-type photocathodes. *J. Mater. Chem. A* **3,** 21990–21994 (2015).

33. Sharma, G. *et al.* Electronic structure, photovoltage, and photocatalytic hydrogen evolution with p-$CuBi_2O_4$ nanocrystals. *J. Mater. Chem. A* **4,** 2936, (2016).

34. Sullivan, I. *et al.* Photoinjection of High Potential Holes into Cu5Ta11O30 Nanoparticles

by Porphyrin Dyes. *J. Phys. Chem. C* **119,** 21294–21303 (2015).

35. Xiong, D. *et al.* Use of delafossite oxides $CuCr_{1-x}Ga_xO_2$ nanocrystals in p-type dye-sensitized solar cell. *J. Alloys Compd.* **662,** 374–380 (2016).

36. Yu, M., Draskovic, T. I. & Wu, Y. Cu(I)-based delafossite compounds as photocathodes in p-type dye-sensitized solar cells. *Phys. Chem. Chem. Phys.* **16,** 5026–5033 (2014).

37. Isayev, O. *et al.* Materials Cartography: Representing and Mining Materials Space Using Structural and Electronic Fingerprints. *Chem. Mater.* **27,** 735–743 (2015).

38. Johnson, M. A. & Maggiora, G. M. *Concepts of Applications of Molecular Similarity*. (John Wiley & Sons, 1990).

39. Balachandran, P. V. & Rajan, K. Structure Maps for $A'_6A''_4(BO_4)_6X_2$ apatites via data mining. *Acta Crystallogr. B.* **68,** 24–33 (2012).

40. Calderon, C. E. *et al.* The AFLOW standard for high-throughput materials science calculations. *Comput. Mater. Sci.* **108,** 233–238 (2015).

41. Bender, A. & Glen, R. C. Molecular similarity: a key technique in molecular informatics. *Org. Biomol. Chem.* **2,** 3204–18 (2004).

42. Johnson, M. A. & Maggiora, G. M. *Concepts and Applications of Molecular Similarity*. (John Wiley & Sons, 1990).

43. Stumpfe, D. & Bajorath, J. Similarity searching. *Wiley Interdiscip. Rev. Comput. Mol. Sci.* **1,** 260–282 (2011).

44. Willett, P. The calculation of molecular structural similarity: Principles and practice. *Mol. Inform.* **33,** 403–413 (2014).

45. Li, Z., Luo, W., Zhang, M., Feng, J. & Zou, Z. Photoelectrochemical cells for solar

hydrogen production: current state of promising photoelectrodes, methods to improve their properties, and outlook. *Energy Environ. Sci.* **6,** 347–370 (2013).

46. Hisatomi, T., Kubota, J. & Domen, K. Recent advances in semiconductors for photocatalytic and photoelectrochemical water splitting. *Chem. Soc. Rev.* **43,** (2014).

47. Yang, K., Setyawan, W., Wang, S., Buongiorno Nardelli, M. & Curtarolo, S. A search model for topological insulators with high-throughput robustness descriptors. *Nat. Mater.* **11,** 614–9 (2012).

48. Frederikse, H. P. R. Permittivity (dielectric constant) of inorganic solids. *CRC Handb. Chem. Physics, 90th Ed. (Internet Version 2010)* 12.44–12–54 (2010).

49. Saliba, M. *et al.* Cesium-containing Triple Cation Perovskite Solar Cells: Improved Stability, Reproducibility and High Efficiency. *Energy Environ. Sci.* **9,** 1989–1997 (2016).

50. Chen, F., Schafranek, R., Li, S., Wu, W. B. & Klein, a. Energy band alignment between $Pb(Zr,Ti)O_3$ and high and low work function conducting oxides—from hole to electron injection. *J. Phys. D. Appl. Phys.* **43,** 295301 (2010).

51. Call, R. W. *et al.* Growth and Post-Deposition Treatments of $SrTiO_3$ Films for Dye Sensitized Photoelectrosynthesis Cell Applications. *ACS Appl. Mater. Interfaces* **8,** 12282–12290 (2016).

52. Mansoor, M. A. *et al.* Perovskite-Structured $PbTiO_3$ Thin Films Grown from a Single-Source Precursor. *Inorg. Chem.* **652,** 5624–5626 (2013).

53. Bhide, V. G., Hegde, M. S. & Deshmukh, K. G. Ferroelectric Properties of Lead Titanate. *J. Am. Ceram. Soc.* **51,** 565–68 (1968).

54. Reitz, C., Leufke, P. M., Hahn, H. & Brezesinski, T. Ordered Mesoporous Thin Film Ferroelectrics of Biaxially Textured Lead Zirconate Titanate (PZT) by Chemical Solution

Deposition. *Chem. Mater.* **26,** 2195–2202 (2014).

55. Varghese, J. *et al.* Fabrication of Arrays of Lead Zirconate Titanate (PZT) Nanodots via Block Copolymer Self-Assembly. *Chem. Mater.* **25,** 1458–1463 (2013).

56. Liu, W., Kong, L., Zhang, L. & Yao, X. Study of the surface layer of lead titanate thin film by X-ray diffraction. *Solid State Commun.* **93,** 653–657 (1995).

57. Qin, P. *et al.* Synthesis and Mechanistic Studies of Organic Chromophores with Different Energy Levels for p-Type Dye-Sensitized Solar Cells. *J. Phys. Chem. C* **114,** 4738–4748 (2010).

58. Qin, P. *et al.* Design of an organic chromophore for P-type dye-sensitized solar cells. *J. Am. Chem. Soc.* **130,** 8570–8571 (2008).

59. Redmond, G. & Fitzmaurice, D. Spectroscopic determination of flatband potentials for polycrystalline titania electrodes in nonaqueous solvents. *J. Phys. Chem.* **97,** 1426–1430 (1993).

60. Won, D. Il *et al.* Highly Robust Hybrid Photocatalyst for Carbon Dioxide Reduction: Tuning and Optimization of Catalytic Activities of Dye/TiO_2/Re(I) Organic-Inorganic Ternary Systems. *J. Am. Chem. Soc.* **137,** 13679–13690 (2015).

61. Watson, D. F. & Meyer, G. J. Cation effects in nanocrystalline solar cells. *Coord. Chem. Rev.* **248,** 1391–1406 (2004).

62. Bella, F. & Grätzel, M. Aqueous dye-sensitized solar cells. *Chem. Soc. Rev.* **44,** 3431–3473 (2015).

63. Law, C. *et al.* Water-based electrolytes for dye-sensitized solar cells. *Adv. Mater.* **22,** 4505–4509 (2010).

64. She, C. *et al.* pH-Dependent Electron Transfer from Re-bipyridyl Complexes to Metal Oxide Nanocrystalline Thin Films. *J. Phys. Chem. B* **109,** 19345–19355 (2005).

65. Cheng, J. *et al.* Efficient Hole Transport Layers with Widely Tunable Work Function for Deep HOMO Level Organic Solar Cells. *J. Mater. Chem. A* **3,** 23955–23963 (2015).

66. Bisquert, J. & Marcus, R. A. Device Modeling of Dye-Sensitized Solar Cells. *Top Curr. Chem* **352,** 325–396 (2014).

67. Lagemaat, J. Van De, Park, N. G. & Frank, A. J. Influence of Electrical Potential Distribution, Charge Transport, and Recombination on the Photopotential and Photocurrent Conversion Efficiency of Dye-Sensitized Nanocrystalline TiO_2 Solar Cells : A Study by Electrical Impedance and Optical Modulation. *J. Phys. Chem. B* **104,** 2044–2052 (2000).